

PointVDP: Learning View-Dependent Projection by Fireworks Rays for 3D Point Cloud Segmentation

Yang Chen, Yueqi Duan, *Member, IEEE*, Haowen Sun, Ziwei Wang,
Jiwen Lu, *Fellow, IEEE*, and Yap-Peng Tan, *Fellow, IEEE*

Abstract—In this paper, we propose view-dependent projection (VDP) to facilitate point cloud segmentation, designing efficient 3D-to-2D mapping that dynamically adapts to the spatial geometry from view variations. Existing projection-based methods leverage view-independent projection in complex scenes, relying on straight lines to generate direct rays or upward curves to reduce occlusions. However, their view independence provides projection rays that are limited to pre-defined parameters by human settings, restricting point awareness and failing to capture sufficient projection diversity across different view planes. Although multiple projections per view plane are commonly used to enhance spatial variety, the projected redundancy leads to excessive computational overhead and inefficiency in image processing. To address these limitations, we design a framework of VDP to generate data-driven projections from 3D point distributions, producing highly informative single-image inputs by predicting rays inspired by the adaptive behavior of fireworks. In addition, we construct color regularization to optimize the framework, which emphasizes essential features within semantic pixels and suppresses the non-semantic features within black pixels, thereby maximizing 2D space utilization in a projected image. As a result, our approach, PointVDP, develops lightweight projections in marginal computation costs. Experiments on S3DIS and ScanNet benchmarks show that our approach achieves competitive results, offering a resource-efficient solution for semantic understanding.

Index Terms—3D Point Cloud Segmentation, 3D-to-2D Mapping, Scene Understanding

I. INTRODUCTION

3D point cloud segmentation tasks aim to segment points in a 3D scene into semantically coherent regions, facilitating scene-level understanding of objects and structures. Abundant methods [1], [2], [3], [4], [5], [6] have explored point-based architectures to process point clouds as sets of points scattering in the 3D domain. Unlike 2D images, 3D point clouds are inherently irregular, sparse, and unordered, posing challenges in feature extraction and representation. To bridge the gap between 3D and 2D domains, some approaches [7], [8], [9] use existing 2D images alongside 3D point cloud datasets, thereby leveraging well-established 2D backbones for robust point

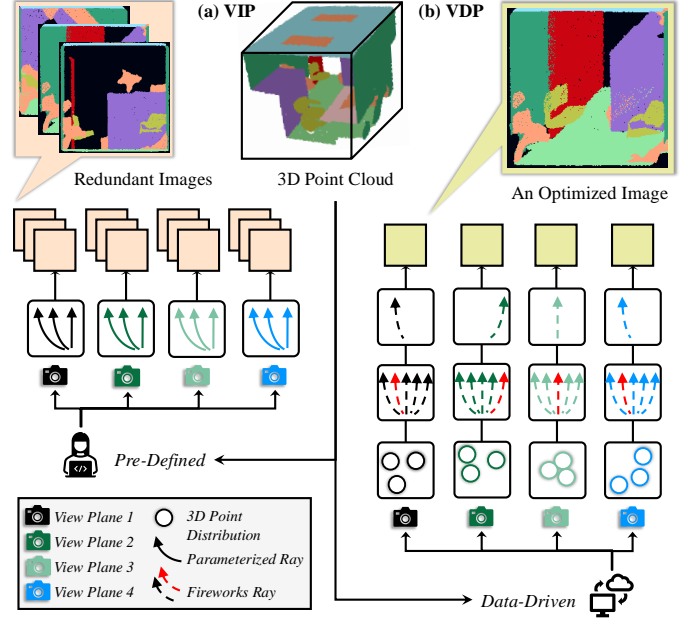


Fig. 1. The view-independent projection (VIP) and view-dependent projection (VDP). From a 3D point cloud, (a) VIP is pre-defined by human settings, where the parameterized rays are fixed for all view planes, relying on multiple and redundant images to capture projection diversity. (b) VDP is a data-driven approach to ingest varied 3D point distribution, which adapts multi-directional fireworks ray for each view plane, predicting the most informative ray on an optimized image. VIP causes redundancy and underutilized 2D space, while VDP enables diversity in marginal computation to advance efficient projection.

cloud understanding. However, these approaches are restricted to scenarios in which the RGB images and 3D scans are jointly collected, and they are not guaranteed in practical settings when faced with datasets lacking explicit 2D modalities. These challenges attract increasing attention on adopting projection-based strategies to convert 3D points into 2D pixels on single object level [10], [11], [12], [13], [14], indoor scene level [15], and outdoor scene level [16], [17].

These projection-based methods typically provide the fixed rays relying on pre-defined parameters in a simplistic scheme, referred to as view-independent projection (VIP). When adapting VIP to environments characterized by denser occlusions and tighter spatial layouts, existing methods develop straight-line rays [10], [11] and upward-curve rays [15] to realize parallel 3D-to-2D mapping and mitigate occluded regions. As illustrated in Fig. 1(a), the fixed rays from VIP are identical across all view planes, which are generated by pre-defined parameters from humanly devised settings. Although the VIP approaches have dedicated physical modeling and extensive empirical

Corresponding author: Yueqi Duan.

Yang Chen, Ziwei Wang, and Yap-Peng Tan are with School of Electrical and Electronic Engineering, Nanyang Technological University, Singapore (e-mail: chen1605@e.ntu.edu.sg; ziwei.wang@ntu.edu.sg; eyptan@ntu.edu.sg).

Yueqi Duan is with the Department of Electronic Engineering, Tsinghua University, Beijing, China (e-mail: duanyueqi@tsinghua.edu.cn).

Haowen Sun and Jiwen Lu are with the Department of Automation, Tsinghua University, Beijing, China (e-mail: sunhw24@mails.tsinghua.edu.cn; lujiwen@tsinghua.edu.cn).

The source code will be made publicly available on GitHub for future research.

analysis, their dependencies on pre-defining parameterized rays involve potential limitations. *First*, VIP causes inefficient space utilization, which includes unnecessary overlapping by high semantic redundancy and resource waste by low 2D space utilization. *Second*, VIP incurs the lack of adaptive variation in 3D point distributions and inherent irregularities among different view planes. As a result, although multiple images per view plane can enable projection diversity, these images are suboptimal for generating repetitive objects, causing non-semantic pixels, and increasing the computational load to accommodate projections of complex structures.

In this paper, we argue that VIP, involving inefficient space utilization and lacking adaptive variation, limits semantic point understanding of spatial representations. The limitations motivate our rethinking of view independence, and we posit that a more effective strategy is to design view dependence. The view dependence aims to predict diverse rays, constructing efficient awareness of space utilization and adaptive variation on local distributions of 3D points. In contrast to view independence, we introduce view dependence with data-driven parameters, from which we propose view-dependent projection (VDP) in Fig. 1(b). Instead of employing a uniform set of rays across all view planes in VIP, VDP is adaptively learned and inferred to embed spatial representations for each view plane. Moreover, instead of adding multiple projected images in VIP, VDP enlarges the diversity of projection rays within a single optimized image, thereby reducing the number of redundant images. Ensuring sufficient projection diversity remains non-trivial. While VDP is data-driven in a point cloud, the projection can converge to an optimal ray limited to global features. Inspired by the fireworks algorithm [18], [19], we develop expansions, integrating the mutation into our pipeline to ensure the projection diversity with local features. Unlike the typical fireworks algorithm that concentrates on continuous searching spaces, we focus on rays mutated among discrete points to mitigate suboptimal clustering and promote broader diversity. Through mutation, we design multi-directional fireworks rays, which boost the expressiveness of view dependence.

To this end, we propose PointVDP to model diverse projections with view dependence through fireworks rays, which adapt to point distributions of varying view planes and generate spatially optimized images. More specifically, we propose a framework of VDP that integrates aggregation, partition, and attention mechanisms to ingest point clouds. Equipped with the mutation, our framework predicts projection rays bouncing from multiple directions. Embedding the framework into an end-to-end pipeline presents optimization challenges, particularly regarding the constraint of projection rays. We design a color regularization strategy, which tackles underutilized 2D space occupied with black pixels to enhance occupancy of semantic pixels. Comprehensive evaluations on the benchmarks, S3DIS [20] and ScanNet [21], demonstrate that PointVDP outperforms many existing methods with efficient processing. Our key contributions are:

- We introduce PointVDP, the first view-dependent projection derived from point distributions. PointVDP is data-driven, which compensates for the shortcomings of pre-defined parameters in view-independent projection.

- In PointVDP, the framework of VDP adapts to spatial structures from varied view planes and captures complex point features. We propose a unique color regularization strategy that contributes to the awareness of 2D space utilization in projected images, effectively predicting fireworks rays to ensure projection diversity.
- PointVDP achieves lightweight input by optimizing the most informative image to replace redundant images, and reserving a fraction of projected images results in marginal computation costs. Our approach is data-driven and resource-effective for advancing projection-based 3D scene understanding.

II. RELATED WORK

A. 3D Scene Segmentation

Existing works develop the deep neural networks to understand 3D point clouds at the scene level, generally containing voxel-based and point-based methods. The voxel-based methods [22], [23], [24] conduct voxelization to divide 3D scenes into cubic voxels and leverage sparse operations to extract features. The point-based methods [25], [26], [27], [28], [29], [30], [31], [32], [2], [3], [4], [5], [33], [1], [34], [35] directly process raw point clouds by using various architectures. Pioneering approaches handle individual points by using the shared multi-layer perceptron (MLP) to aggregate global features [6] and using hierarchical structures for local spatial relations [25]. Building on the MLP-based philosophy, subsequent methods focus on refining training strategies [1], designing novel blocks [3], and developing multi-resolution learning [36]. Moreover, convolutional kernels [29], [30], [26], graph structures [28], [37], [38], [39] and transformer-based architectures [27], [32], [4], [5], [40] are designed for scene analysis. Despite their effectiveness, the methods are commonly applied for embedding learning in the 3D domain, and there are still performance gaps of irregular points compared with regular pixels in images. Our method achieves 3D scene segmentation with guidance in the 2D domain by considering the point distributions across individual view planes.

B. Point Cloud Analysis with 2D Guidance

In the 3D point cloud analysis, leveraging guidance from 2D pre-trained backbone achieves remarkable progress. Some methods typically leverage comprehensive datasets that process additional real-world images paired with precise camera pose information [41], [8], [7], [42]. Concurrent with these methods, projection-based methods only ingest 3D points and derive 2D features by projecting 3D points onto 2D view planes [13], [14], [17], [16], [10], [11], [43], [12], [15]. For example, multi-view projections create 2D representations, such as PointClip [11], TAP [12], MVCNN [13], and MVTN [14] on 3D object level, RangeFormer [16] and RangeViT [17] on 3D outdoor scene level, and MirageRoom [15] on 3D indoor scene level. However, these projection-based methods are built on view independence, relying on pre-defined parameters from human settings. As a result, their parameterized rays have limited availability of different view planes, which remain a significant bottleneck for further advancement in dynamically

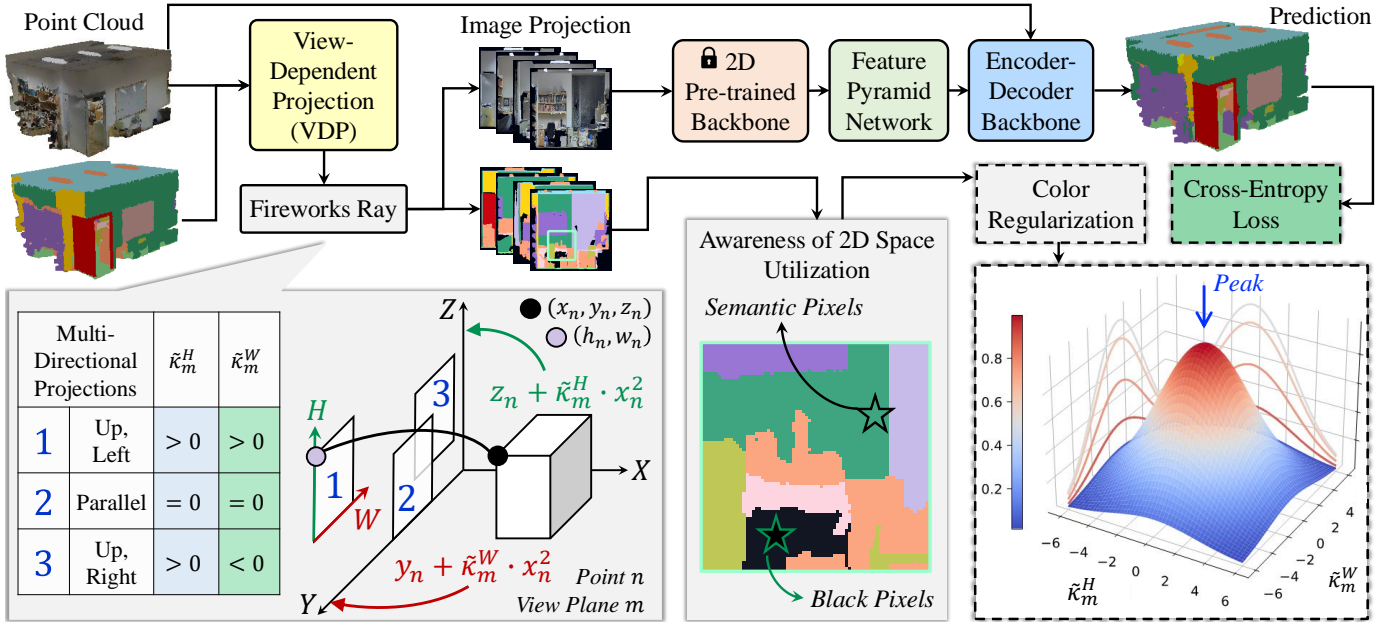


Fig. 2. The pipeline of our PointVDP. Our pipeline is composed of a framework of view-dependent projection (VDP) to ingest 3D point cloud for generating representative embeddings of point distributions, where the detailed framework is illustrated in Fig. 3. This framework dynamically predicts diverse fireworks rays, which perform multi-directional projections under different view plans. The projected images contain two color schemes, where the real-color images are processed through 2D pre-trained backbone, feature pyramid network, and encoder-decoder backbone, extracting 2D features fused with 3D features for semantic prediction. For semantic-color images, we conduct awareness of 2D space utilization to detect non-semantic black pixels and develop color regularization to optimize images, thereby boosting the segmentation performance.

adapting to various point distributions. In contrast to view independence, we propose a generalized framework of view dependence that produces data-driven projections.

C. Fireworks Algorithm

The fireworks algorithm [44] is first conceptualized from the natural phenomenon of fireworks, sparking in the night sky to illuminate surrounding areas. In this algorithm, fireworks are simulated as feasible sparks, which are generated to distribute throughout a search space of an optimization problem. Multiple variants have been proposed to enhance the algorithm with in-depth analyses, theoretical foundations, and practical applications [18]. Many existing works focus on refining spark generation, mutation operators, mapping rules, and selection strategies to better handle high-dimensional and multi-modal problems. For instance, EFWA [45] introduces mutation operators that enhance local search capabilities, whereas a further work [19] proposes an improved Gaussian sparks operator, which dynamically adjusts spark distributions for more robust performance. Beyond the foundational studies, the fireworks algorithm is widely used in optimization design [46], optimal scheduling [47], pattern recognition [48], and other diverse domains because of its high precision and fast convergence, balancing local mining and global exploration. Despite its success, the dynamic nature of fireworks algorithm continues to inspire novel solutions in complex scenarios, and we explore this algorithm on 3D points to mutate diverse projections.

III. PROPOSED METHOD

In this paper, we present PointVDP to learn view-dependent projections (VDP) from a 3D point cloud. Unlike the view-

independent projections (VIP) in prior works, PointVDP enhances the diversity of projections at a view level. The rest of this section is organized as follows. We begin with introducing the overall pipeline of our PointVDP in Section III-A. In Section III-B, we introduce our projection strategy, which contains revisiting VIP, proposing VDP, framework of VDP, and fireworks ray from VDP. We develop our optimization strategy in Section III-C, including boundary constraint, awareness of 2D space utilization, and color regularization.

A. Overall Pipeline

We illustrate the overall pipeline of PointVDP in Fig. 2. The input is a 3D point cloud $P = (X, Y, Z) \in \mathbb{R}^{N \times 3}$ with N points, where a point $p_n = (x_n, y_n, z_n) \in P$ has 3 dimensions. Our view-dependent projection converts the 3D point cloud to 2D view planes. Suppose the point p_n is mapped to YZ view plane, we generate its projected location (h_n, w_n) to form a pixel $I(h_n, w_n)$ of an image $I \in \mathbb{R}^{H \times W \times 3}$, where H is the height and W is the width with 3-dim (R, G, B) channels. The 3D-to-2D mapping projects points in point clouds under the XYZ axes to pixels in images under the HW axes.

3D point cloud P has real colors scanned by 3D sensors and semantic colors from GroundTruth labels. To ensure the projection diversity, we develop PointVDP in Section III-B to generate 2D projected images. First, real-color projected images are ingested for training and inference. We use two 2D pre-trained backbones, Swin Transformer [49] and SGFormer [50] pre-trained on ImageNet-1K [51] to encode 2D features, aggregating multi-level features by a Feature Pyramid Network [52]. Following MirageRoom [15], 3D point-wise features are generated through the encoder-decoder backbone

and fused with 2D features by the masked reprojection module. Second, semantic-color projected images are only conducted during training as supervision signals, from which we design color regularization based on the awareness of 2D space utilization in Section III-C to optimize training.

B. Projection Strategy

1) *Revisiting View-Independent Projection (VIP)*: Typical straight-line projections and upward-curve projections are view-independent projections. Straight-line projection [10], [11] is the most straightforward method to project a 3D point from (x_n, y_n, z_n) to (h_n, w_n) . The formulation is:

$$\begin{aligned} h_n &= \frac{z_n - \min(Z)}{\max(Z) - \min(Z)} H, \\ w_n &= \frac{y_n - \min(Y)}{\max(Y) - \min(Y)} W, \end{aligned} \quad (1)$$

where it depicts parallel rays along X axis to reach to YZ view plane as the second parallel example in Fig. 1. This projection omits the X axis, so front objects lead to occlusions on behind objects, hindering projections from exposing sufficient points and resulting in ineffective point-wise features. Recent advancement of upward-curve projection, known as mirage projection [15], leverages the mirage phenomenon to distort rays over the ground. Based on physical modeling, this projection modifies (1) by reformulating z_n with a parameterized function as:

$$z_n + \kappa \cdot x_n^2, \quad (2)$$

where κ denotes non-negative parameters to control the ray with a height in vertical dimension. Note that zero κ indicates straight lines, while positive κ considers depth x_n along X axis in 3D, from which the behind objects have higher positions to be exposed along the H axis in a 2D image. In VIP, the pre-defined parameters, *i.e.*, $\kappa \in \{0, 1, 2\}$, lead to parameterized rays fixed for all view planes.

2) *Proposing View-Dependent Projection (VDP)*: We argue that such VIP only generates fixed projections and neglects the unique point distribution of different view planes. In contrast to VIP, we consider view-dependent projection (VDP) based on the limitations of VIP and motivations of VDP.

Limitations of VIP. The pre-defined κ in (2) enforces all view planes with the same projection rays, which has limitations because different view planes have various situations. Moreover, the projection only considers the depth X for height Z , but omits the depth X for the width Y . We argue that for the YZ view plane, the Z axis decides the H dimension and the Y axis decides the W dimension of an image, where the remaining X axis denotes the depth, thereby resulting in incomplete distortions for the vertical H and horizontal W dimensions through the current approach. Besides, all curves only have an upward direction under image coordinates. As a result, the projection is generally fixed, and each plane has the same κ , forcing the same view of the height direction.

Motivations of VDP. Considering that point distributions have variability across each view plane, we propose VDP, which projects data-driven rays to substitute pre-defined rays. Inspired by the behavior of fireworks rays in the real world,

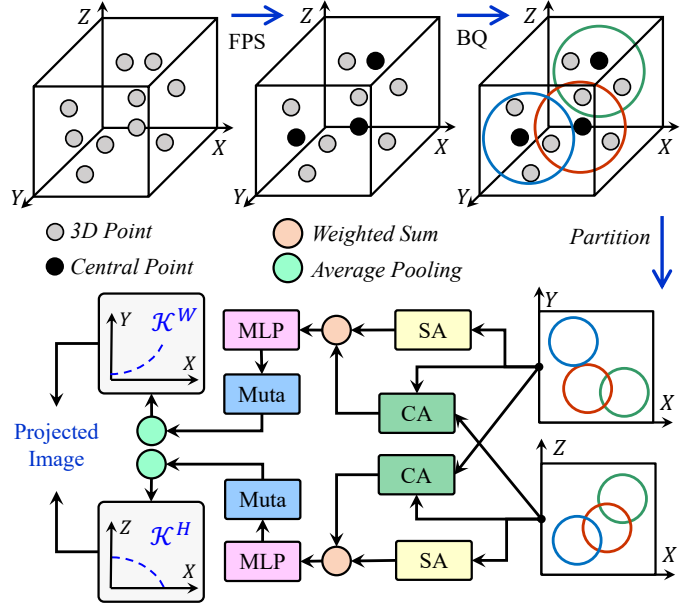


Fig. 3. Framework of view-dependent projection (VDP). Our PointVDP is composed of a framework of VDP to ingest 3D point cloud through Farthest Point Sampling (FPS) and Ball Query (BQ), conducting aggregation on central points. We develop partition to generate representative embeddings of point distributions under different view planes. To embed spatial information, we conduct Self-Attention (SA), Cross-Attention (CA), MLP, and Mutation (Muta) blocks to predict dynamic and diverse rays for projected images.

we advance the dynamic diversity from all directions, from which our approach is aware of point distributions under XZ axes of the H dimension and XY axes of the W dimension, respectively. To achieve the data-driven approach of our VDP, we design a dynamic framework, which is a lightweight network to generate firework rays by ingesting point distributions, and we demonstrate the details as follows.

3) *Framework of View-Dependent Projection (VDP)*: To conduct view-dependent projection across multiple views, we index each view plane as $m = 1, 2, \dots, M$ for a 3D point cloud. A view plane m has the related set of sub-points defined as P^m from the raw point cloud P . Suppose we select the right normal direction with X at the positive axis of the YZ view plane, the partial points set for projection is $P^m = \{P = (X, Y, Z) \mid X > 0\}$. In general, P^m is a large set of points resulting in computational complexity when leveraged as input. To ingest and reflect P^m , we design a framework as VDP as shown in Fig. 3, containing aggregation, partition, attention, and mutation blocks.

Aggregation. To design a lightweight framework, we proceed with P^m to representative subsets by aggregating overlapping partitions of points. To standardize the subsets, we select S central points in P^m by the farthest point sampling, where each central point $p_s^m \in P^m$ is indexed by $s = 1, 2, \dots, S$. Based on the location of each central point p_s^m , we defined a neighborhood ball through radius r in the Euclidean space by the ball query algorithm as:

$$\Theta_s = \text{Pooling}(\text{BallQuery}(p_s^m)), \quad (3)$$

where each ball is a patch with a different number of points and we use the pooling operator to calculate the mean of 3D

positions of each ball. For view plane m , it has S balls defined as $\{\Theta_s\}_{s=1}^S \in \mathbb{R}^{S \times 3}$ from all central points, which can evenly cover the whole set P^m . There exists overlapping among balls.

Partition. We abstract the position information from balls, where each 3-dim $\Theta_s = (X_s, Y_s, Z_s)$ contains positions from XYZ axes. We conduct partition on Θ_s by XZ , XY , and YZ view planes, which corresponds to H and W dimensions in a 2D image. To generate 2-dim representative embeddings, we develop concatenation as \oplus :

$$\{\Theta_s^{XY}, \Theta_s^{XZ}\} = \{X_s \oplus Y_s, X_s \oplus Z_s\}. \quad (4)$$

Attention. Based on balls, we develop self-attention blocks $\text{SA}(\cdot)$ and cross-attention blocks $\text{CA}(\cdot)$ across view planes:

$$\begin{aligned} \{\mu_s^{\dot{H}}, \mu_s^{\dot{W}}\} &= \{\text{SA}(\Theta_s^{XZ}, \Theta_s^{XZ}), \text{SA}(\Theta_s^{XY}, \Theta_s^{XY})\}, \\ \{\mu_s^{\ddot{H}}, \mu_s^{\ddot{W}}\} &= \{\text{CA}(\Theta_s^{XZ}, \Theta_s^{XY}), \text{CA}(\Theta_s^{XY}, \Theta_s^{XZ})\}, \end{aligned} \quad (5)$$

where we separately calculate the embeddings for H and W dimensions a balanced weight ω to adjust the combination between the same and different view planes as:

$$\{\mu_s^H, \mu_s^W\} = \omega \cdot \{\mu_s^{\dot{H}}, \mu_s^{\dot{W}}\} + (1 - \omega) \cdot \{\mu_s^{\ddot{H}}, \mu_s^{\ddot{W}}\}. \quad (6)$$

We leverage $\mu_s = \{\mu_s^H, \mu_s^W\}$ as the output to process dynamic rays, where the output forms the sets as $\{\mu_s^H\}_{s=1}^S \in \mathcal{U}_m^H$ and $\{\mu_s^W\}_{s=1}^S \in \mathcal{U}_m^W$ for all S balls of the view plane m . Furthermore, we leverage a lightweight linear block following the attention blocks:

$$\{\kappa_m^H, \kappa_m^W\} = \text{Pooling}(\text{MLP}(\{\mathcal{U}_m^H, \mathcal{U}_m^W\})), \quad (7)$$

where the average pooling converts the set of S balls into to $\kappa_m = \{\kappa_m^H, \kappa_m^W\}$.

Mutation. Inspired and different from fireworks algorithm, we develop our algorithm on individual points in 3D domain. More specifically, we design a mutation strategy $\text{Muta}(\cdot)$ to develop the diversity of fireworks rays, from which we develop diverse projections from varying points. To ensure the dynamic diversity of projection rays, κ_m is simultaneously processed through mutation strategy $\text{Muta}(\cdot)$ as depicted in Algorithm 1 as:

$$\{\tilde{\kappa}_m^H, \tilde{\kappa}_m^W\} = \text{Muta}(\{\kappa_m^H, \kappa_m^W\}), \quad (8)$$

where $\tilde{\kappa}_m = \{\tilde{\kappa}_m^H, \tilde{\kappa}_m^W\}$. To qualify the diversity of rays, we define an upper bound $\hat{\kappa}$ and a lower bound $\check{\kappa}$ as boundaries to restrict the projections.

Algorithm 1 The process of mutation $\text{Muta}(\cdot)$ in PointVDP.

Input: κ_m , upper bound $\hat{\kappa}$, lower bound $\check{\kappa}$

- 1: **for** each view plane m in M **do**
 - 2: Generate dynamic mutation $\text{Gaussian}(0, 1)$
 - 3: Calculate $\tilde{\kappa}_m = \kappa_m \cdot (1 + \text{Gaussian}(0, 1))$
 - 4: **if** $\tilde{\kappa}_m > \hat{\kappa}$ or $\tilde{\kappa}_m < \check{\kappa}$ **then**
 - 5: $\tilde{\kappa}_m = \check{\kappa} + |\tilde{\kappa}_m| \% (\hat{\kappa} - \check{\kappa})$
 - 6: **end if**
 - 7: **end for**
-

4) *Fireworks ray from View-Dependent Projection (VDP):* Our framework of VDP generates diverse rays. We obtain rays from multiple directions controlled by both H and W dimensions as $\mathcal{K}^H = \{\tilde{\kappa}_m^H\}_{m=1}^M$ and $\mathcal{K}^W = \{\tilde{\kappa}_m^W\}_{m=1}^M$ in (8) for M view planes. Fig. 2 depicts that the learnable \mathcal{K}^H and \mathcal{K}^W further generate multi-directional projections, thereby realizing diverse rays, which are data-driven based on point distributions. Compared with pre-defined projections, our data-driven projections advance semantic understanding. \mathcal{K}^H and \mathcal{K}^W are sets containing diverse rays of M view planes for a 3D point cloud. Moreover, κ_m^H and κ_m^W are rational numbers across positive, zero, and negative values. The mutated $\tilde{\kappa}_m^H \in \mathcal{K}^H$ and $\tilde{\kappa}_m^W \in \mathcal{K}^W$ further provide diverse rays, dynamically controlling the projections from all directions. Therefore, we develop a multi-directional distortion for the YZ view plane, which effectively generates images based on the unique point distribution of each view plane m to fit various points. The diverse sets \mathcal{K}^H and \mathcal{K}^W are learnable for all M view planes of different 3D point clouds. Therefore, from view plane $m \rightarrow \tilde{\kappa}_m = \{\tilde{\kappa}_m^H, \tilde{\kappa}_m^W\}$, we design (h_n, w_n) as:

$$\begin{aligned} h_n &= \frac{z_n + \tilde{\kappa}_m^H \cdot x_n^2 - \min(Z)}{\max(Z) - \min(Z)} H, \\ w_n &= \frac{y_n + \tilde{\kappa}_m^W \cdot x_n^2 - \min(Y)}{\max(Y) - \min(Y)} W. \end{aligned} \quad (9)$$

In general, current approaches leverage multiple images per view plane, causing semantic redundancy with repeated objects and computational consumptions. Besides, there exist low-quality images with large regions of black pixels without providing semantic information. These redundant and non-semantic results motivate us to reduce the number of images by optimizing the most informative projection per view plane as a single image for processing. Therefore, we design the optimization strategy of fireworks rays as follows.

C. Optimization Strategy

1) *Boundary Constraint:* To optimize the fireworks rays, we first qualify the boundary constraints of all projections. We provide toy examples and evaluate the projection diversity from two aspects, 2D image visualization with projection diversity in Fig. 4 and boundary of height and width in Table I. We analyze 6 settings of the firework rays through data-driven projections of our VDP, and typical rays are indexed by (a), (b), (c), (d), (e), (f). As shown in Fig. 4, we provide detailed 2D projected images of a point cloud generated by (a) as straight-line ray, (b) as upward-curve ray, (c) as downward-leftward-curve ray, (d) as upward-leftward-curve ray, (e) as downward-rightward curve ray, and (f) as upward-rightward curve rays. We project diverse images based on the same view plane. It is clear that with the help of our data-driven projection, more objects can be projected onto the image plane. For example, there are fewer black pixels in (d) than (b), which indicates that more semantic pixels appear without changing the view plane and the point exposure. Meanwhile, as we attempt diverse rays, more objects with new semantic classes appear, such as the red door in (f) compared with (b). Thus, VDP provides high-quality images with more semantic information for 2D

TABLE I

ANALYSIS OF PROJECTION DIVERSITY. BASED ON THE TOY EXAMPLE IN FIG. 4, WE REPORT THE DIRECTION OF FIREWORKS RAYS, WHERE \uparrow , \downarrow , \leftarrow , AND \rightarrow INDICATE UPWARD, DOWNWARD, LEFTWARD, AND RIGHTWARD RAYS. FOR PROJECTED IMAGES ON THE YZ VIEW PLANE WITH THE SIDE OF $X \geq 0$, WE DEVELOP BOUNDARY CONSTRAINTS OF HEIGHT FOR THE XZ VIEW PLANE AND WIDTH FOR THE XY VIEW PLANE. WE ALSO ANALYZE THE PROJECTION DIVERSITY FROM THE AWARENESS OF 2D SPACE UTILIZATION AND COLOR REGULARIZATION.

| Image in Fig. 4 | Direction of Fireworks Ray | H | H | W | W | Boundary Constraint XZ View Plane (Height) | Boundary Constraint XY View Plane (Width) | Awareness in (10) | Regularization in (11) |
|-----------------|------------------------------|--------------|--------------|--------------|---------------|---|---|----------------------|---------------------------|
| | | \uparrow | \downarrow | \leftarrow | \rightarrow | | | | |
| (a) | Straight-Line Ray | X | X | X | X | $z_n \leq \max(Z)$ | $y_n \leq \max(Y)$ | 37.1% | 0.88 |
| (b) | Upward-Curve Ray | \checkmark | X | X | X | $z_n + \tilde{\kappa}_m^H x_n^2 \leq \max(Z)$ | $y_n \leq \max(Y)$ | 72.2% | 0.52 |
| (c) | Downward-Leftward-Curve Ray | X | \checkmark | \checkmark | X | $z_n + \tilde{\kappa}_m^H x_n^2 \geq \min(Z)$ | $y_n + \tilde{\kappa}_m^W x_n^2 \leq \max(Y)$ | 77.8% | 0.49 |
| (d) | Upward-Leftward-Curve Ray | \checkmark | X | \checkmark | X | $z_n + \tilde{\kappa}_m^H x_n^2 \leq \max(Z)$ | $y_n + \tilde{\kappa}_m^W x_n^2 \leq \max(Y)$ | 85.3% | 0.45 |
| (e) | Downward-Rightward-Curve Ray | X | \checkmark | X | \checkmark | $z_n + \tilde{\kappa}_m^H x_n^2 \geq \min(Z)$ | $y_n + \tilde{\kappa}_m^W x_n^2 \geq \min(Y)$ | 80.2% | 0.48 |
| (f) | Upward-Rightward-Curve Ray | \checkmark | X | X | \checkmark | $z_n + \tilde{\kappa}_m^H x_n^2 \leq \max(Z)$ | $y_n + \tilde{\kappa}_m^W x_n^2 \geq \min(Y)$ | 74.5% | 0.50 |

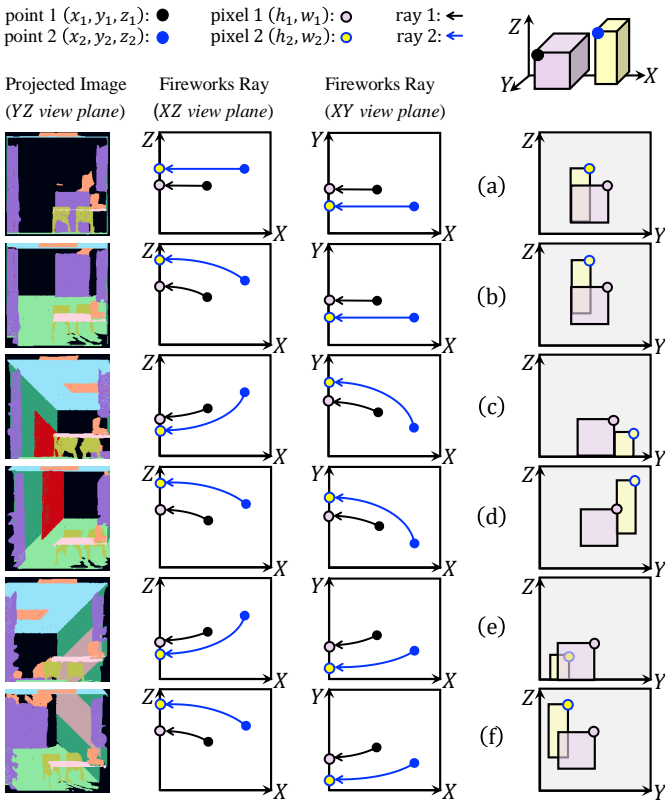


Fig. 4. Toy example of fireworks ray. Our framework of VDP predicts diverse rays from 3D points to 2D projected images, realizing the projection diversity. We generate the 2D image visualization based on various projection rays indexed with (a), (b), (c), (d), (e), (f). Suppose a point cloud with 2 objects under the XYZ axes. From the YZ view plane, we define 2 points, where the front object has ray 1 projecting point 1 (x_1, y_1, z_1) to pixel 1 (h_1, w_1) and the behind object has ray 2 projecting point 2 (x_2, y_2, z_2) to pixel 2 (h_2, w_2) . The fireworks rays, including ray 1 and ray 2, have decompositions in the H dimension under the XZ view plane and the W dimension under the XY view plane. Note that H and W are the axes of the 2D images that are parallel to the Z and Y axes.

feature extraction. From these images, the notation $n \in \{1, 2\}$ in Table I indicates 2 objects and m indexes view plane, where $\max(\cdot)$ is 0.5 and $\min(\cdot)$ is -0.5 for XYZ axes based on the point cloud processing. For projected images on the YZ view plane with the side of $X \geq 0$, we constrain boundaries of height for the XZ view plane and width for the XY view plane.

2) *Awareness of 2D Space Utilization*: We propose 2D space utilization, a term to evaluate the occupancy of semantic pixels, while on the contrary, non-semantic pixels are black pixels. In general, black pixels are derived from ineffective projections without any points along the rays. We color a image \bar{I} based on GroundTruth and calculate its 2D space utilization U_{Space} as:

$$U_{Space} = \left(\frac{\sum_{h_n=1}^H \sum_{w_n=1}^W 1\{\bar{I}(h_n, w_n) > \vec{0}\}}{H \cdot W} \right)^\tau, \quad (10)$$

where the normalized $\bar{I} \in \mathbb{R}^{H \times W \times 3}$ corresponds to its real-color image I defined in the preliminary and τ is a tuning parameter to control the level of awareness. A pixel $\bar{I}(h_n, w_n)$ is defined as a black pixel if it has zero value as $\vec{0} = (0, 0, 0)$ for 3-dim (R, G, B) channels, while the remaining semantic pixels have positive values. The (h_n, w_n) is generated through the dynamic approach in (9), so U_{Space} of each possible projected image is different, and we generate a single projection by leveraging U_{Space} into a regularization strategy to achieve lightweight input. We further calculate the 2D space utilization for a toy example in Table I, demonstrating that (c), (d), (e), (f) outperform (a), (b) with increased U_{Space} . We desire a higher U_{Space} , which means an image containing less non-semantic information in (10). Through the awareness of 2D space utilization, our framework of VDP is optimized to generate better projections for images, covering more black pixels to provide efficient inputs for 2D processing.

3) *Color Regularization*: To optimize the training of the framework of VDP, we conduct color regularization by leveraging U_{Space} in (10) as the standard deviation of a two-dimensional Gaussian kernel as:

$$l(\tilde{\kappa}_m^H, \tilde{\kappa}_m^W) = \frac{1}{\sqrt{2\pi} \cdot U_{Space}} \cdot \exp\left(-\frac{(\tilde{\kappa}_m^H)^2 + (\tilde{\kappa}_m^W)^2}{2 \cdot (U_{Space})^2}\right), \quad (11)$$

where a large standard deviation indicates a high 2D space utilization with fewer black pixels, generating a small regularization to penalize the prediction. The Gaussian kernel is a symmetric bell-shaped curve, and we illustrate its 3D plot in Fig. 2. We design a color regularization strategy for the predicted $\tilde{\kappa}_m = \{\tilde{\kappa}_m^H, \tilde{\kappa}_m^W\}$. We observe that the peak of the symmetric bell-shaped curve is $1/(\sqrt{2\pi} \cdot U_{Space})$ at the 2-dim center with $(\tilde{\kappa}_m^H, \tilde{\kappa}_m^W) = (0, 0)$. The peak leads to maximal regularization due to inefficient 2D space utilization, and the regularization gradually decreases with larger absolute values

TABLE II

PERFORMANCE OF 3D SEMANTIC SEGMENTATION ON S3DIS [20] AND SCANNET [21]. WE REPORT OA (%), mACC (%), AND mIoU (%) WITH GPU USAGE AND LEARNABLE PARAMETERS. WE DEMONSTRATE THE INPUT MODALITY: 3D *only* INDICATES ONLY LEVERAGING 3D WITHOUT 2D; 3D & 2D INDICATES LEVERAGING BOTH 3D AND 2D WHERE 2D COLLECTED IMAGES ARE ATTACHED WITH 3D DATASETS; 3D → 2D INDICATES LEVERAGING 3D WHERE 2D PROJECTED IMAGES ARE GENERATED FROM 3D. WE RETRAIN THE BASELINE AND EVALUATE OUR METHOD BASED ON TWO PRE-TRAINED BACKBONES, WHERE THE ORIGINAL BACKBONE IS SWIN-T AND THE CHANGED BACKBONE IS SG-FORMER-S ANNOTATED WITH A SUPERScript (+*SG*).

| Method | GPUs Usage | OA (%) | S3DIS mAcc (%) | mIoU (%) | ScanNet mIoU (%) | Learnable Parameters | Input Modality |
|---------------------------|------------|--------------------|--------------------|--------------------|--------------------|----------------------|----------------------------|
| PointNet++ [25] | 1×12G | 83.0 | - | 53.5 | 53.3 | 1.0M | 3D <i>only</i> |
| KPConv [29] | - | - | 72.8 | 67.1 | 69.2 | 15.0M | 3D <i>only</i> |
| JSENet [53] | 1×12G | - | - | 67.7 | 69.9 | 16.2M | 3D <i>only</i> |
| Point Transformer v1 [31] | 4×24G | 90.8 | 76.5 | 70.4 | 70.6 | 7.8M | 3D <i>only</i> |
| Point Transformer v2 [54] | 4×24G | 91.1 | 77.9 | 71.6 | 75.4 | 12.8M | 3D <i>only</i> |
| Point Transformer v3 [55] | 8×24G | - | - | 74.7 | 78.6 | 46.2M | 3D <i>only</i> |
| PointNeXt [1] | 1×32G | 90.6 | 76.8 | 70.5 | 71.5 | 41.6M | 3D <i>only</i> |
| RepSurf-U [56] | - | 90.2 | 76.0 | 68.9 | 70.0 | 1.0M | 3D <i>only</i> |
| PointMetaBase [3] | 1×32G | 90.8 | - | 71.3 | 72.8 | 19.7M | 3D <i>only</i> |
| SPoTr [5] | - | 90.7 | 76.4 | 70.8 | - | 1.7M | 3D <i>only</i> |
| HGNet [37] | - | 90.7 | 76.9 | 70.8 | - | 7.8M | 3D <i>only</i> |
| PointDif [4] | 1×24G | - | 77.1 | 70.0 | - | - | 3D <i>only</i> |
| BPNet [7] | - | - | - | - | 73.9 | - | 3D & 2D (UNet [57]) |
| MVPNet [8] | 1×12G | - | - | - | 65.0 | 1.0M | 3D & 2D (VGG16 [58]) |
| MirageRoom [15] | 1×24G | 87.2 | 68.4 | 61.8 | 60.4 | 5.8M | 3D → 2D (Swin-T [49]) |
| PointVDP | 1×24G | 90.0 (+2.8) | 74.1 (+5.7) | 67.8 (+6.0) | 69.7 (+9.3) | 5.8M | 3D → 2D (Swin-T [49]) |
| MirageRoom(+ <i>SG</i>) | 1×24G | 90.1 | 74.1 | 68.2 | 70.3 | 5.6M | 3D → 2D (SG-Former-S [50]) |
| PointVDP(+ <i>SG</i>) | 1×24G | 90.7 (+0.6) | 76.5 (+2.4) | 71.0 (+2.8) | 72.1 (+1.8) | 5.6M | 3D → 2D (SG-Former-S [50]) |

on $(\tilde{\kappa}_m^H, \tilde{\kappa}_m^W)$, indicating a higher utilization rate of 2D space. Table I reports the relevant settings with 2D space utilization and the peak of color regularization for different projected images. A higher U_{Space} means an optimized image with more semantic pixels, and we assign a lower peak of color regularization as $l(0, 0)$ in (11). In addition, we further summarize the regularization of the predicted $\tilde{\kappa}_m = \{\tilde{\kappa}_m^H, \tilde{\kappa}_m^W\}$ for all $m = 1, 2, \dots, M$ view planes as:

$$L_{Sparks} = \sum_{m=1}^M l(\tilde{\kappa}_m^H, \tilde{\kappa}_m^W). \quad (12)$$

The 3D point cloud segmentation assigns labels for individual points, regularizing predicted label \tilde{l}_i based on GroundTruth label l_i for each of the n points within C classes in point clouds. We adopt a widely-used L_{ce} :

$$L_{ce} = \frac{-1}{n \cdot C} \sum_{i=1}^n \sum_{c=1}^C l_{i,c} \cdot \log\left(\frac{\exp(\tilde{l}_{i,c})}{\sum_{c=1}^C \exp(\tilde{l}_{i,c})}\right), \quad (13)$$

where L_{ce} is the cross-entropy loss. Based on the proposed color regularization, the overall optimization is formulated as:

$$L = L_{ce} + \lambda \cdot L_{Sparks}, \quad (14)$$

where λ is a balanced weight, and our pipeline is under joint training to realize the 3D point cloud segmentation.

IV. EXPERIMENT

We elaborate on the experimental setting in Section IV-A, and present the results that include overall segmentation performance, time complexity, space complexity, class-wise IoU performance, and qualitative visualization in Section IV-B. Moreover, we ablate different projection rays, design choices, and sensitivity of parameters in Section IV-C.

TABLE III

MODEL EFFICIENCY OF TIME COMPLEXITY AND SPACE COMPLEXITY ON S3DIS [20]. WE EVALUATE TIME USAGE (MIN) AND SPEED (MS/SAMPLE) AS THE TIME COMPLEXITY DURING TRAINING AND INFERENCE. WE ALSO REPORT THE MEMORY USAGE (G) PER 24G GPU, THE MAXIMUM BATCH SIZE, AND THE IMAGE NUMBER PER 3D SCENE DURING TRAINING.

| Method | Time Complexity | | | | Space Complexity | | |
|--------------------------|-----------------|-------|-----------|-------|------------------|-------|-------|
| | Training | | Inference | | Training | | |
| | Time | Speed | Time | Speed | Memory | Batch | Image |
| MirageRoom [15] | 5400 | 529 | 210 | 322 | 19.6 | 1 | 12 |
| PointVDP | 3720 | 365 | 120 | 184 | 23.8 | 3 | 4 |
| MirageRoom(+ <i>SG</i>) | 3360 | 329 | 102 | 157 | 22.7 | 3 | 12 |
| PointVDP(+ <i>SG</i>) | 3060 | 300 | 90 | 138 | 23.5 | 6 | 4 |

A. Experimental Setting

1) *Datasets and Evaluation Metrics*: We conduct experiments on 3D scene datasets, S3DIS [20] and ScanNet [21]. S3DIS covers 271 rooms in 6 areas with 13 classes, where Area 5 is for inference and others are for training. ScanNet contains 1613 cluttered indoor scenes annotated with 20 classes, which are split into 1201 training scans, 312 validation scans, and 100 test scans. We evaluate our methods on three metrics: OA (%), mACC (%), and mIoU (%). OA is the overall accuracy, mACC is the mean accuracy within each class, and mIoU is the mean intersection over union.

2) *Model Architectures*: Our framework of VDP has MLP feature channel numbers as 2, 9, and 1 with Sigmoid activation. We set input resolution of projected images as 224, and the following resolutions are 56, 28, and 14. To ingest projected images, we adopt 3 layers of Swin-T [49] as the 2D pre-trained backbone, where it is pre-trained on ImageNet-

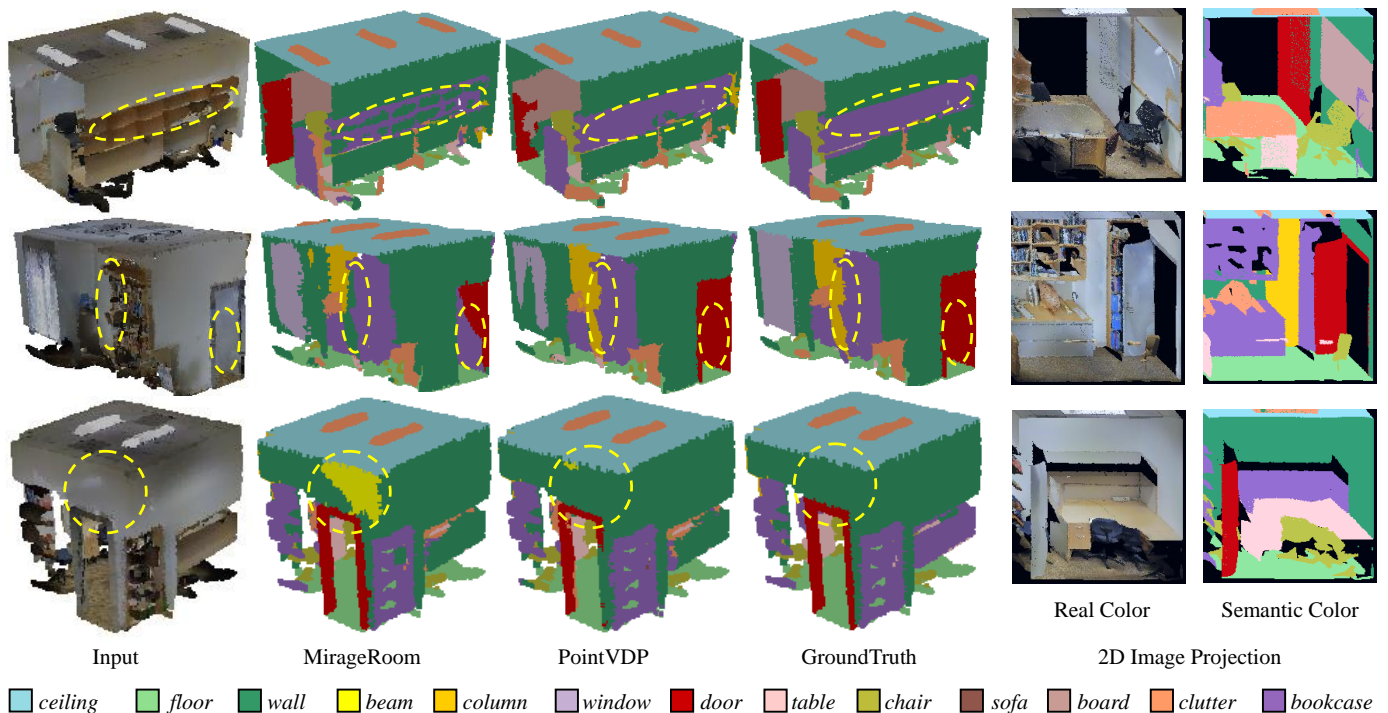


Fig. 5. Visualization of 3D semantic segmentation on S3DIS [20]. We illustrate the qualitative results from left to right, including the input, MirageRoom, PointVDP, and GroundTruth in the 3D domain with relevant image projection of real color and semantic color in the 2D domain.

TABLE IV

THE CLASS-WISE SEMANTIC SEGMENTATION RESULTS OF S3DIS [20] DATASET. WE REPORT CLASS-WISE IOU (%) FOR ALL 13 SEMANTIC CLASSES, THOROUGHLY COMPARING OUR METHOD WITH THE BASELINE BASED ON TWO 2D PRE-TRAINED BACKBONES. WE INDICATE THE PERFORMANCE IMPROVEMENTS (\uparrow), DECLINES (\downarrow), OR CONSTANTS (\leftrightarrow).

| Method | mIoU | ceiling | floor | wall | beam | column | window | door | table | chair | sofa | bookcase | board | clutter |
|-----------------------|----------------|------------------|------------------|----------------|-------------------|-----------------|-------------------|-----------------|----------------|----------------|-----------------|----------------|----------------|------------------|
| MirageRoom [15] | 61.8 | 88.8 | 98.4 | 79.7 | 0.0 | 20.4 | 60.1 | 56.7 | 80.8 | 87.7 | 44.2 | 72.1 | 66.3 | 48.0 |
| PointVDP | 67.8 | 93.4 | 98.5 | 82.5 | 0.0 | 35.5 | 46.0 | 67.4 | 85.9 | 91.6 | 71.7 | 75.9 | 75.4 | 58.1 |
| Differential Analysis | $\uparrow 6.0$ | $\uparrow 4.6$ | $\uparrow 0.1$ | $\uparrow 2.8$ | \leftrightarrow | $\uparrow 15.1$ | $\downarrow 14.1$ | $\uparrow 10.7$ | $\uparrow 5.1$ | $\uparrow 3.9$ | $\uparrow 27.5$ | $\uparrow 3.8$ | $\uparrow 9.1$ | $\uparrow 10.1$ |
| MirageRoom(+ SG) | 68.2 | 95.1 | 98.7 | 81.9 | 0.0 | 34.4 | 50.4 | 66.1 | 83.4 | 91.8 | 70.3 | 74.6 | 79.4 | 60.9 |
| PointVDP(+ SG) | 71.0 | 94.9 | 98.6 | 83.4 | 0.3 | 34.9 | 58.5 | 72.0 | 85.1 | 93.6 | 79.3 | 76.9 | 84.9 | 60.2 |
| Differential Analysis | $\uparrow 2.8$ | $\downarrow 0.2$ | $\downarrow 0.1$ | $\uparrow 1.5$ | $\uparrow 0.3$ | $\uparrow 0.5$ | $\uparrow 8.1$ | $\uparrow 6.9$ | $\uparrow 1.7$ | $\uparrow 1.8$ | $\uparrow 9.0$ | $\uparrow 2.3$ | $\uparrow 5.5$ | $\downarrow 0.7$ |

1K [51] with 27.5M fixed parameters. The feature pyramid network (FPN) generates feature maps, involving input channels as 192, 384, and 768, and output channels aligning with encoder channels. We adopt the same segmentation backbone in MirageRoom [15], which has 3 encoder layers with channel numbers as 96, 192, and 384. The 2D pre-trained backbone of our approach is Swin-T [49], and we further substitute it with a lightweight SG-Former-S [50]. SG-Former-S [50] has 21.8M fixed parameters and changes the FPN input channels to 64, 128 and 256, from which we use a superscript (+ SG) for discrimination. Therefore, it is worth noting that we separately conduct 2 groups of comparisons: the proposed PointVDP and the backbone MirageRoom based on Swin-T [49], and the proposed PointVDP(+ SG) and the backbone MirageRoom(+ SG) based on SG-Former-S [50].

3) *Implementation Details*: All experiments are conducted on a 24G RTX 3090 GPU with the PyTorch toolkit. We perform training processes for 100 epochs through the AdamW optimizer with a learning rate of 0.006. The weight decay is

0.05 for both datasets. We set the number of view planes M as 4 for each scene to generate fireworks rays. We retrain the baseline using $\kappa \in \{0, 1, 2\}$ to align with the original settings of VIP to project images. For the framework of VDP in the proposed PointVDP, we set the number of central points S of FPS as 32, the radius r of BQ as 0.2, and the weight ω of attention as 0.8. The upper and lower bounds are κ_a as 5 and κ_b as -5 for mutation. The tuning parameter τ is 0.8 for S3DIS and 0.4 for ScanNet. The balanced weight λ of loss is 0.2 for S3DIS and 0.3 for ScanNet.

B. Results

1) *Semantic Segmentation Results on S3DIS and ScanNet*: The baseline is reported using four 48G GPUs, achieving OA/mAcc/mIoU as 91.3%/78.2%/72.0% on S3DIS and mIoU as 74.9% on ScanNet. For fair comparisons, we retrain the baseline and our proposed method using a 24G GPU. We show the results of our method and recent state-of-the-art methods in

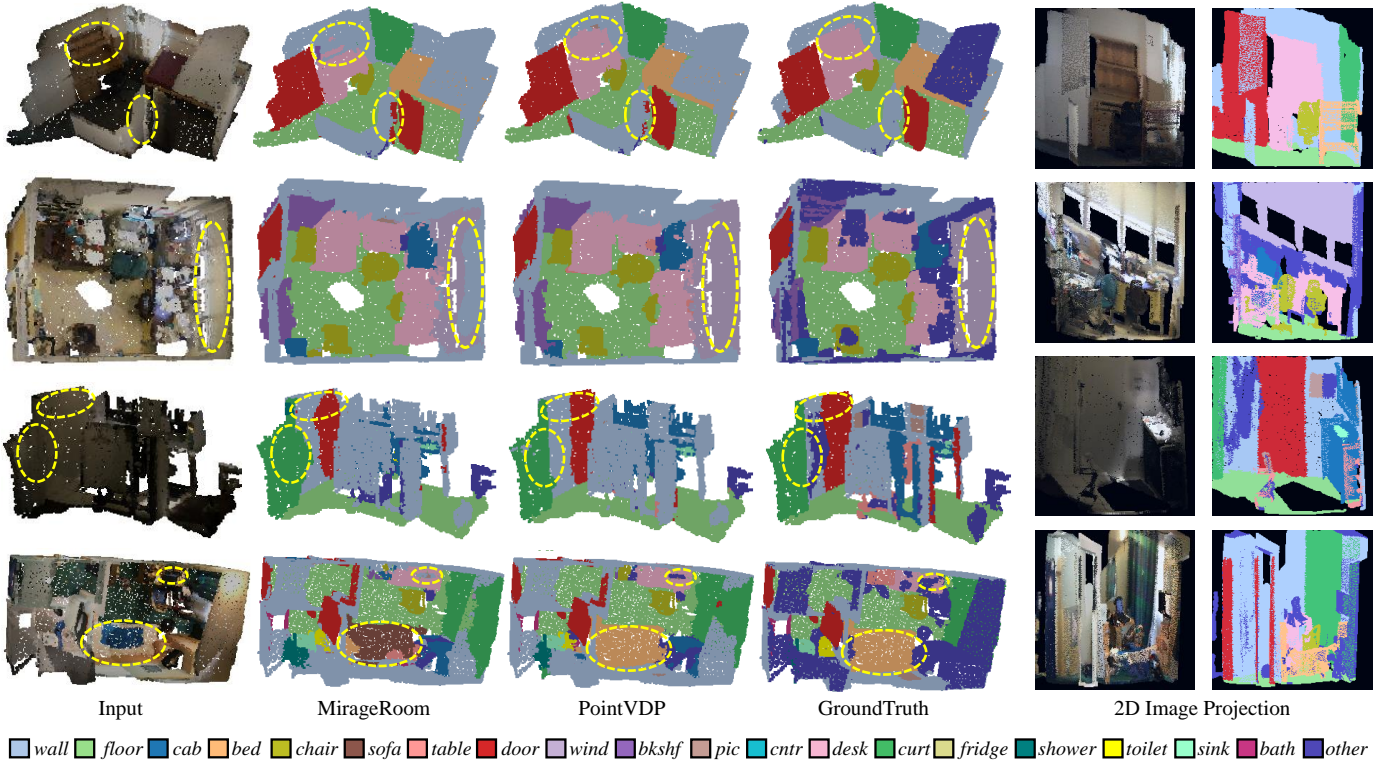


Fig. 6. Visualization of 3D semantic segmentation on ScanNet [21]. We illustrate the qualitative results from left to right, including the input, MirageRoom, PointVDP, and GroundTruth in the 3D domain with relevant image projection of real color and semantic color in the 2D domain.

TABLE V

THE CLASS-WISE SEMANTIC SEGMENTATION RESULTS OF SCANNET [21] DATASET. WE REPORT CLASS-WISE IOU (%) FOR ALL 20 SEMANTIC CLASSES, THOROUGHLY COMPARING OUR METHOD WITH THE BASELINE BASED ON TWO 2D PRE-TRAINED BACKBONES. WE INDICATE THE PERFORMANCE IMPROVEMENTS (\uparrow), DECLINES (\downarrow), OR CONSTANTS (\leftrightarrow).

| Method | mIoU | wall | floor | cab | bed | chair | sofa | table | door | wind | bkshf | pic | cntr | desk | curt | fridge | shower | toilet | sink | bath | other |
|-----------------------------|----------------|----------------|----------------|-----------------|-----------------|-------------------|------------------|----------------|-----------------|-----------------|-----------------|----------------|----------------|----------------|------------------|-----------------|----------------|----------------|----------------|-------------------|-----------------|
| MirageRoom [15] | 60.4 | 79.8 | 94.4 | 53.5 | 56.2 | 84.6 | 70.9 | 60.3 | 51.4 | 51.8 | 63.9 | 24.4 | 59.7 | 51.7 | 66.9 | 40.3 | 45.2 | 84.7 | 57.2 | 73.6 | 37.7 |
| PointVDP | 69.7 | 84.3 | 96.2 | 64.0 | 78.4 | 88.9 | 79.7 | 72.0 | 63.9 | 63.0 | 74.7 | 32.9 | 63.6 | 60.1 | 65.1 | 58.6 | 54.4 | 92.7 | 63.3 | 88.1 | 50.3 |
| Differential Analysis | $\uparrow 9.3$ | $\uparrow 4.5$ | $\uparrow 1.8$ | $\uparrow 10.5$ | $\uparrow 22.2$ | $\uparrow 4.3$ | $\uparrow 8.8$ | $\uparrow 7.7$ | $\uparrow 12.5$ | $\uparrow 11.2$ | $\uparrow 10.8$ | $\uparrow 8.5$ | $\uparrow 3.9$ | $\uparrow 8.4$ | $\downarrow 1.8$ | $\uparrow 18.3$ | $\uparrow 9.2$ | $\uparrow 8.0$ | $\uparrow 6.1$ | $\uparrow 14.5$ | $\uparrow 12.6$ |
| MirageRoom ^(+SG) | 70.3 | 84.4 | 96.2 | 65.8 | 80.4 | 89.9 | 83.3 | 72.2 | 65.4 | 61.6 | 76.8 | 33.0 | 61.9 | 61.1 | 72.0 | 54.7 | 54.8 | 91.9 | 63.1 | 87.7 | 50.1 |
| PointVDP ^(+SG) | 72.1 | 84.8 | 96.3 | 65.9 | 81.5 | 89.9 | 83.0 | 73.4 | 65.5 | 62.6 | 79.6 | 34.5 | 63.5 | 62.7 | 75.1 | 59.6 | 63.2 | 93.8 | 66.4 | 87.7 | 52.8 |
| Differential Analysis | $\uparrow 1.8$ | $\uparrow 0.4$ | $\uparrow 0.1$ | $\uparrow 0.1$ | $\uparrow 1.1$ | \leftrightarrow | $\downarrow 0.3$ | $\uparrow 1.2$ | $\uparrow 0.1$ | $\uparrow 1.0$ | $\uparrow 2.8$ | $\uparrow 1.5$ | $\uparrow 1.6$ | $\uparrow 1.6$ | $\uparrow 3.1$ | $\uparrow 4.9$ | $\uparrow 8.4$ | $\uparrow 1.9$ | $\uparrow 3.3$ | \leftrightarrow | $\uparrow 2.7$ |

Table II. As the model architectures explained in Section IV-A, our method depicts the improved segmentation results of the proposed PointVDP and PointVDP^(+SG) compared with the baseline MirageRoom and MirageRoom^(+SG), where the superscript ^(+SG) means a different 2D re-trained backbone. It is important to note that the 2D pre-trained backbone used in ^(+SG) is more lightweight with a higher classification result, where SG-Former-S [50] achieves 83.2% and Swin-T [49] achieves 81.2% on ImageNet-1K [51]. Based on the advantage, our PointVDP^(+SG) significantly outperforms our PointVDP for the 3D semantic segmentation task on S3DIS and ScanNet. We compare the baseline and our proposed method from 2 groups within the same backbones. *First*, PointVDP outperforms MirageRoom with 2.8%/5.7%/6.0% in terms of the OA/mAcc/mIoU on the test set Area 5 of S3DIS dataset. We also report mIoU on the validation set of ScanNet. Our PointVDP improves MirageRoom by 9.3%.

These results indicate that our proposed VDP method provides more informative projections compared with the existing VIP method. *Second*, for S3DIS dataset, our PointVDP^(+SG) further achieves competitive performances on all three metrics as 90.7%, 76.5%, and 71.0% with small amounts of learnable parameters compared with other existing methods. By using limited computing resources, our PointVDP^(+SG) achieves 72.1%, which outperforms MirageRoom^(+SG) and completes promising segmentation. Based on a reduced number of parameters as 5.6M, our method outperforms many recently proposed methods.

2) *Time Complexity and Space Complexity*: We outline the time complexity and space complexity of the baseline models and the proposed models in Table III, and all efficiency metrics are measured across the S3DIS dataset. We compare 2 different 2D pre-trained backbones for 4 methods, including MirageRoom, PointVDP, MirageRoom^(+SG), and PointVDP^(+SG).

For time complexity, we calculate the time usage and speed to evaluate the model efficiency during the training and inference procedures, and our approach maintains reasonable efficiency. For space complexity, we report memory consumption, the maximum batch size, and the number of 2D projected images. More images introduce more computations, where the baseline constructs 12 images per scene. We generate 4 optimal images, thereby achieving a decrease of $1 - (4/12) = 66.7\%$. The decreased image number directly leads to an increased batch size. Our training process on the original baseline is finished with a maximum batch size of 1. We achieve dynamically diverse projections by PointVDP, so the demands of projected images are reduced with an increased batch size of 3. Then, we substitute a lightweight 2D pre-trained backbone to increase the batch size of baseline to 3 and PointVDP^(+SG) to 6. Besides, we compare the model size and GPU demand. The previous method is conducted on $4 \times 48\text{G}$ GPUs, and our lightweight method uses $1 \times 24\text{G}$ GPU. Thus, the computation cost is reduced by $1 - (24/(4 \times 48)) = 87.5\%$. As a result, our method reduces projected images by 66.7%, which achieves lightweight input for 2D feature processing. Moreover, we reduce the computation costs by 87.5% and achieve comparable results compared with the original baseline method.

3) *Class-wise IoU Performance*: Based on overall mIoU results, we thoroughly analyze class-wise IoU results of S3DIS in Table IV and ScanNet in Table V. We evaluate our proposed method and the baseline, comparing PointVDP with MirageRoom, and PointVDP^(+SG) with MirageRoom^(+SG). Our method achieves higher IoUs on most semantic classes, where PointVDP^(+SG) has the best results on 10 out of 13 semantic classes of S3DIS and 17 out of 20 semantic classes of ScanNet. We demonstrate performance improvements, declines, or constants of our methods compared with the baseline. For example, PointVDP^(+SG) shows 10 best results on S3DIS including *wall* ($\uparrow 1.5\%$), *beam* ($\uparrow 0.3\%$), *column* ($\uparrow 0.5\%$), *window* ($\uparrow 8.1\%$), *door* ($\uparrow 6.9\%$), *table* ($\uparrow 1.7\%$), *chair* ($\uparrow 1.8\%$), *sofa* ($\uparrow 9.0\%$), *bookcase* ($\uparrow 2.3\%$), and *board* ($\uparrow 5.5\%$). Meanwhile, compared with MirageRoom^(+SG), PointVDP^(+SG) has improvements on *table* ($\uparrow 1.2\%$), *bkshf* ($\uparrow 2.8\%$), *fridge* ($\uparrow 4.9\%$), *sink* ($\uparrow 3.3\%$), and many other classes for ScanNet. We conclude that the class-wise improvements are consistent in different dataset selections.

4) *Qualitative Visualization*: To provide intuitive comparisons, we visualize semantic segmentation results on challenging scenes. Fig. 5 and Fig. 6 present the performances of S3DIS and ScanNet datasets. It is important to note that our comparisons are based on the ^(+SG) backbone. Starting from the leftmost figure and moving to the right, the results contain the visualizations of the input scene, baseline, proposed method, and GroundTruth results. Taking the real color and semantic color as references, we also provide the related 2D image projection from the inner part of each 3D scene. We use the yellow dashed circles to highlight our improvements. Compared with the baseline, our method performs better with a leading performance, which also gradually aligns with the GroundTruth result. For example, our method boosts the segmentation on *wall*, *door*, and *bookcase* for S3DIS, as well as *wall*, *bed*, *wind*, and *desk* for ScanNet. These improvements

TABLE VI
ABLATION OF THE FRAMEWORK OF VDP. WE EXPLAIN THE DESIGN CHOICES AND REPORT THE mAcc (%) AND mIoU (%) RESULTS.

| Framework of VDP | mAcc (%) | mIoU (%) |
|---|------------|------------|
| Aggregation + Partition + Attention (Vanilla) | 74.6 | 69.2 |
| + Mutation | 75.1(+0.5) | 70.3(+1.1) |
| + Color Regularization | 76.5(+1.4) | 71.0(+0.7) |

TABLE VII
ABLATION OF PRE-DEFINED AND DATA-DRIVEN PROJECTION. THE MULTIPLE DIRECTIONS (\uparrow , \downarrow , \leftarrow , \rightarrow) CONTAINING UPWARD, DOWNWARD, LEFTWARD, AND RIGHTWARD ARE REPORTED WITH mAcc (%) AND mIoU (%), AND WE HIGHLIGHT THE PRE-DEFINED AND DATA-DRIVEN PROJECTIONS. FOR EACH VIEW PLANE m , WE DEMONSTRATE THE IMAGE NUMBER.

| ID | Image Num per m | H \uparrow | H \downarrow | W \leftarrow | W \rightarrow | mAcc (%) | mIoU (%) |
|-----|-------------------|--------------|----------------|----------------|-----------------|----------|----------|
| (1) | 3 | ✓ | ✗ | ✗ | ✗ | 74.1 | 68.2 |
| (2) | 2 | ✓ | ✗ | ✗ | ✗ | 74.4 | 68.8 |
| (3) | 1 | ✓ | ✗ | ✗ | ✗ | 74.1 | 68.9 |
| (4) | 1 | ✓ | ✗ | ✗ | ✗ | 75.3 | 69.6 |
| (5) | 1 | ✓ | ✗ | ✗ | ✗ | 74.9 | 69.0 |
| (6) | 1 | ✓ | ✗ | ✗ | ✗ | 75.6 | 70.0 |
| (7) | 1 | ✓ | ✓ | ✓ | ✓ | 75.7 | 70.0 |
| (8) | 1 | ✓ | ✓ | ✓ | ✓ | 76.5 | 71.0 |

validate the effectiveness of our method, and we achieve better or more comparative results on challenging benchmarks.

C. Ablations

We further design ablations to mainly investigate the effects with various combinations of design choices. All experiments are conducted on the PointVDP^(+SG) model for S3DIS and ScanNet datasets.

1) *Effectiveness of the Framework of VDP*: To verify the architecture design of our framework, we conduct ablations on S3DIS. We first introduce a vanilla framework that conducts aggregation, partition, and attention to generate feature embeddings from XY and XZ view planes. We further consider mutation from the fireworks algorithm to ensure the diversity of projection rays. Finally, we optimize the framework through a color regularization strategy. As shown in Table VI, the mutation boosts the vanilla in terms of mAcc (+0.5%) and mIoU (+1.1%). Our exploration provides guidance for the framework of VDP to optimize learning with total increases by 1.9% in mAcc and 1.8% in mIoU, improving the segmentation performance.

2) *Comparison of Pre-Defined and Data-Driven Projection*: Instead of the pre-defined rays and upward-only directions proposed by VIP approaches, our VDP approach designs data-driven rays predicted by the framework of VDP, where the rays spread from multiple directions. As shown in Table VII, the pre-defined projection from VIP leverages fixed κ for each view plane m , which neglects the variation of point distributions. In detail, the IDs of (1)(2)(3)(4) are upward rays defined with $k \in \{0, 1, 2\}$, $k \in \{0, 1\}$, $k = 0.2$, and $k = 1$, respectively. In contrast, the data-driven projection from VDP leverages a general family of functions to enable

TABLE VIII
ABLATION OF THE LEVEL ON THE AWARENESS OF 2D SPACE UTILIZATION, WHERE WE REPORT OA (%), mACC (%), AND mIoU (%).

| U_{Space} | $\tau = 1.0$ | $\tau = 0.8$ | $\tau = 0.6$ | $\tau = 0.4$ | $\tau = 0.2$ | $\tau = 0.0$ |
|-------------|--------------|--------------|--------------|--------------|--------------|--------------|
| OA (%) | 90.0 | 89.9 | 90.1 | 90.3 | 90.0 | 89.7 |
| mAcc (%) | 79.2 | 78.9 | 79.3 | 80.0 | 79.4 | 78.6 |
| mIoU (%) | 71.1 | 70.8 | 71.0 | 72.1 | 70.9 | 70.4 |

TABLE IX
ABLATION OF THE BALANCED LOSS WEIGHT FOR TRAINING REGULARIZATION. WE REPORT OA (%), mACC (%), AND mIoU (%).

| S3DIS | | | | | | |
|----------|-----------------|------------------|------------------|-----------------|-----------------|-----------------|
| Loss | $\lambda = 0.0$ | $\lambda = 0.01$ | $\lambda = 0.02$ | $\lambda = 0.1$ | $\lambda = 0.2$ | $\lambda = 1.0$ |
| OA (%) | 91.1 | 90.2 | 91.0 | 90.9 | 90.7 | 90.5 |
| mAcc (%) | 76.8 | 75.5 | 76.1 | 75.4 | 76.5 | 75.3 |
| mIoU (%) | 70.9 | 69.9 | 70.6 | 70.0 | 71.0 | 70.2 |
| ScanNet | | | | | | |
| Loss | $\lambda = 0.0$ | $\lambda = 0.2$ | $\lambda = 0.3$ | $\lambda = 0.5$ | $\lambda = 0.7$ | $\lambda = 0.8$ |
| OA (%) | 89.8 | 90.0 | 90.4 | 90.1 | 90.1 | 90.2 |
| mAcc (%) | 78.7 | 79.2 | 79.9 | 79.1 | 79.6 | 79.3 |
| mIoU (%) | 70.4 | 71.1 | 71.4 | 70.6 | 71.1 | 71.0 |

the diversity of all M view planes, where $\mathcal{K}^H = \{\tilde{\kappa}_m^H\}_{m=1}^M$ for H dimension and $\mathcal{K}^W = \{\tilde{\kappa}_m^W\}_{m=1}^M$ for W dimension of each 3D scene. We conduct several random runs for data-driven projection, where the IDs of (5)(6) are fixed with $\tilde{\kappa}_m^H \geq 0$ and $\tilde{\kappa}_m^W = 0$. The IDs of (7)(8) are diverse fireworks rays, allowing $\tilde{\kappa}_m^H$ and $\tilde{\kappa}_m^W$ across positive, zero, and negative values. The best result of the pre-defined projection is 69.6% with κ being 1, while the data-driven projection achieves a better result that surpasses it by 2.4% in mIoU.

3) *Level on Awareness of 2D Space Utilization:* Table VIII provides ablations on ScanNet, focusing on levels for 2D space utilization controlled by τ . We report 6 levels, including the original level with $\tau = 1.0$, low level with $\tau = 0.8$, medium-low level with $\tau = 0.6$, medium-high level with $\tau = 0.4$, high level with $\tau = 0.2$, and full level with $\tau = 0.0$. The 2D space utilization is expected to be more scalable regarding the standard deviation of the Gaussian kernel, from which we refine our model design to strengthen awareness. Compared with all levels, we have obtained optimal results increased by 90.3%/80.0%/72.1% in terms of OA/mAcc/mIoU in the medium-high level across all settings.

4) *Loss Weight of Color Regularization:* We formulate the training regularization with a weight λ in (14). To verify the robustness, we evaluate λ in Table IX on S3DIS and ScanNet, where λ balances the regularization between L_{ce} and L_{Sparks} . We observe that our method is not sensitive to hyper-parameters, where different settings do not cause significant fluctuations, indicating that our method has stability.

V. CONCLUSION

In this paper, we propose PointVDP, a data-driven approach to conduct the view-dependent projection, tailored for unique point distributions of different view planes to advance point

cloud understanding. Our framework of VDP predicts the fireworks rays to ensure the projection diversity. We develop color regularization to optimize the framework through awareness of 2D space utilization, minimizing non-semantic regions for the most informative image and generating high-quality 2D features to be fused with 3D features. Experimental results on 3D scene datasets show that our approach achieves comparable performance in marginal computation costs.

Limitations and future work. PointVDP conducts diverse projections on the plane level, and we aim to delve deeper into the object level and point level in our future exploration. In addition, our approach is limited to indoor scene segmentation, and the extension to adopting data-driven projections in outdoor scene segmentation is promising.

ACKNOWLEDGMENT

This work is supported in part by the NTU Start up Grant 024303-00001, in part by the National Research Foundation of Singapore under the NRF Medium Sized Centre Scheme (CARTIN), and in part by the National Natural Science Foundation of China under Grant 62206147.

REFERENCES

- [1] G. Qian, Y. Li, H. Peng, J. Mai, H. Hammoud, M. Elhoseiny, and B. Ghanem, "Pointnext: Revisiting pointnet++ with improved training and scaling strategies," *NeurIPS*, pp. 23 192–23 204, 2022.
- [2] J. Choe, C. Park, F. Rameau, J. Park, and I. S. Kweon, "Point-mixer: Mlp-mixer for point cloud understanding," in *ECCV*, 2022, pp. 620–640.
- [3] H. Lin, X. Zheng, L. Li, F. Chao, S. Wang, Y. Wang, Y. Tian, and R. Ji, "Meta architecture for point cloud analysis," in *CVPR*, 2023, pp. 17 682–17 691.
- [4] X. Zheng, X. Huang, G. Mei, Y. Hou, Z. Lyu, B. Dai, W. Ouyang, and Y. Gong, "Point cloud pre-training with diffusion models," in *CVPR*, 2024, pp. 22 935–22 945.
- [5] J. Park, S. Lee, S. Kim, Y. Xiong, and H. J. Kim, "Self-positioning point-based transformer for point cloud understanding," in *CVPR*, 2023, pp. 21 814–21 823.
- [6] C. R. Qi, H. Su, K. Mo, and L. J. Guibas, "Pointnet: Deep learning on point sets for 3D classification and segmentation," in *CVPR*, 2017, pp. 652–660.
- [7] W. Hu, H. Zhao, L. Jiang, J. Jia, and T.-T. Wong, "Bidirectional projection network for cross dimension scene understanding," in *CVPR*, 2021, pp. 14 373–14 382.
- [8] M. Jaritz, J. Gu, and H. Su, "Multi-view pointnet for 3D scene understanding," in *ICCVW*, 2019, pp. 0–0.
- [9] S. Tianfang, Z. Zhizhong, T. Xin, Q. Yanyun, and X. Yuan, "Image understands point cloud: Weakly supervised 3D semantic segmentation via association learning," *IEEE TIP*, 2024.
- [10] R. Zhang, L. Wang, Y. Qiao, P. Gao, and H. Li, "Learning 3D representations from 2D pre-trained models via image-to-point masked autoencoders," in *CVPR*, 2023, pp. 21 769–21 780.
- [11] R. Zhang, Z. Guo, W. Zhang, K. Li, X. Miao, B. Cui, Y. Qiao, P. Gao, and H. Li, "Pointclip: Point cloud understanding by clip," in *CVPR*, 2022, pp. 8552–8562.
- [12] Z. Wang, X. Yu, Y. Rao, J. Zhou, and J. Lu, "Take-a-photo: 3D-to-2D generative pre-training of point cloud models," in *ICCV*, 2023, pp. 5640–5650.
- [13] H. Su, S. Maji, E. Kalogerakis, and E. Learned-Miller, "Multi-view convolutional neural networks for 3D shape recognition," in *ICCV*, 2015, pp. 945–953.
- [14] A. Hamdi, S. Giancola, and B. Ghanem, "Mvtn: Multi-view transformation network for 3D shape recognition," in *ICCV*, 2021, pp. 1–11.

- [15] H. Sun, Y. Duan, J. Yan, Y. Liu, and J. Lu, "Mirageroom: 3D scene segmentation with 2D pre-trained models by mirage projection," in *CVPR*, 2024, pp. 20 237–20 246.
- [16] L. Kong, Y. Liu, R. Chen, Y. Ma, X. Zhu, Y. Li, Y. Hou, Y. Qiao, and Z. Liu, "Rethinking range view representation for lidar segmentation," in *ICCV*, 2023, pp. 228–240.
- [17] A. Ando, S. Gidaris, A. Bursuc, G. Puy, A. Boulch, and R. Marlet, "Rangevit: Towards vision transformers for 3D semantic segmentation in autonomous driving," in *CVPR*, 2023, pp. 5240–5250.
- [18] J. Li and Y. Tan, "A comprehensive review of the fireworks algorithm," *CSUR*, vol. 52, no. 6, pp. 1–28, 2019.
- [19] J. Guo and W. Liu, "Enhanced fireworks algorithm with an improved gaussian sparks operator," in *ISICA*, 2019, pp. 38–49.
- [20] I. Armeni, S. Sax, A. R. Zamir, and S. Savarese, "Joint 2D-3D-semantic data for indoor scene understanding," *arXiv preprint arXiv:1702.01105*, 2017.
- [21] A. Dai, A. X. Chang, M. Savva, M. Halber, T. Funkhouser, and M. Nießner, "ScanNet: Richly-annotated 3D reconstructions of indoor scenes," in *CVPR*, 2017, pp. 5828–5839.
- [22] C. Choy, J. Gwak, and S. Savarese, "4D spatio-temporal convnets: Minkowski convolutional neural networks," in *CVPR*, 2019, pp. 3075–3084.
- [23] X. Lai, Y. Chen, F. Lu, J. Liu, and J. Jia, "Spherical transformer for lidar-based 3D recognition," in *CVPR*, 2023, pp. 17 545–17 555.
- [24] H. Zhou, X. Zhu, X. Song, Y. Ma, Z. Wang, H. Li, and D. Lin, "Cylinder3d: An effective 3D framework for driving-scene lidar semantic segmentation," *arXiv preprint arXiv:2008.01550*, 2020.
- [25] C. R. Qi, L. Yi, H. Su, and L. J. Guibas, "Pointnet++: Deep hierarchical feature learning on point sets in a metric space," *NeurIPS*, vol. 30, 2017.
- [26] W. Wu, Z. Qi, and L. Fuxin, "Pointconv: Deep convolutional networks on 3D point clouds," in *CVPR*, 2019, pp. 9621–9630.
- [27] M.-H. Guo, J.-X. Cai, Z.-N. Liu, T.-J. Mu, R. R. Martin, and S.-M. Hu, "Pct: Point cloud transformer," *CVM*, pp. 187–199, 2021.
- [28] L. Landrieu and M. Simonovsky, "Large-scale point cloud semantic segmentation with superpoint graphs," in *CVPR*, 2018, pp. 4558–4567.
- [29] H. Thomas, C. R. Qi, J.-E. Deschaud, B. Marcotegui, F. Goulette, and L. J. Guibas, "Kpconv: Flexible and deformable convolution for point clouds," in *ICCV*, 2019, pp. 6411–6420.
- [30] M. Xu, R. Ding, H. Zhao, and X. Qi, "Paconv: Position adaptive convolution with dynamic kernel assembling on point clouds," in *CVPR*, 2021, pp. 3173–3182.
- [31] H. Zhao, L. Jiang, J. Jia, P. H. Torr, and V. Koltun, "Point transformer," in *ICCV*, 2021, pp. 16 259–16 268.
- [32] C. Park, Y. Jeong, M. Cho, and J. Park, "Fast point transformer," in *CVPR*, 2022, pp. 16 949–16 958.
- [33] Y. Chen, Y. Duan, R. Zhang, and Y.-P. Tan, "Adaptive margin contrastive learning for ambiguity-aware 3D semantic segmentation," in *ICME*, 2024.
- [34] H. Shuai, X. Xu, and Q. Liu, "Backward attentive fusing network with local aggregation classifier for 3D point cloud semantic segmentation," *IEEE TIP*, vol. 30, pp. 4973–4984, 2021.
- [35] F. Yang, X. Li, and J. Shen, "Nested architecture search for point cloud semantic segmentation," *IEEE TIP*, vol. 32, pp. 2889–2900, 2022.
- [36] Y. Zheng, X. Xu, J. Zhou, and J. Lu, "Pointras: Uncertainty-aware multi-resolution learning for point cloud segmentation," *IEEE TIP*, vol. 31, pp. 6002–6016, 2022.
- [37] T. Yao, Y. Li, Y. Pan, and T. Mei, "Hgnet: Learning hierarchical geometry from points, edges, and surfaces," in *CVPR*, 2023, pp. 21 846–21 855.
- [38] A. Tao, Y. Duan, Y. Wei, J. Lu, and J. Zhou, "Seggroup: Seg-level supervision for 3D instance and semantic segmentation," *IEEE TIP*, vol. 31, pp. 4952–4965, 2022.
- [39] Y. Zheng, J. Lu, Y. Duan, and J. Zhou, "Structural relation modeling of 3D point clouds," *IEEE TIP*, 2024.
- [40] Y. Duan, H. Sun, J. Yan, J. Lu, and J. Zhou, "Learning cross-attention point transformer with global porous sampling," *IEEE TIP*, 2024.
- [41] Z. Wang, Y. Rao, X. Yu, J. Zhou, and J. Lu, "Semaffinet: Semantic-affine transformation for point cloud segmentation," in *CVPR*, 2022, pp. 11 819–11 829.
- [42] M. Rong, H. Cui, and S. Shen, "Efficient 3D scene semantic segmentation via active learning on rendered 2D images," *IEEE TIP*, vol. 32, pp. 3521–3535, 2023.
- [43] Z. Wang, X. Yu, Y. Rao, J. Zhou, and J. Lu, "P2p: Tuning pre-trained image models for point cloud analysis with point-to-pixel prompting," *NeurIPS*, vol. 35, pp. 14 388–14 402, 2022.
- [44] Y. Tan and Y. Zhu, "Fireworks algorithm for optimization," in *ICSI*, 2010, pp. 355–364.
- [45] S. Zheng, A. Janecek, and Y. Tan, "Enhancing the performance of fireworks algorithm using mutation operators," in *IEEE CEC*, 2013, pp. 2069–2077.
- [46] R. Cheng, Y. Bai, Y. Zhao, X. Tan, and T. Xu, "Improved fireworks algorithm with information exchange for function optimization," *KBS*, vol. 163, pp. 82–90, 2019.
- [47] L. He, W. Li, Y. Zhang, and Y. Cao, "A discrete multi-objective fireworks algorithm for flowshop scheduling with sequence-dependent setup times," *SEC*, vol. 51, p. 100575, 2019.
- [48] M. Zhang, Y. Yuan, R. Wang, and W. Cheng, "Recognition of mixture control chart patterns based on fusion feature reduction and fireworks algorithm-optimized msvm," *PAA*, vol. 23, no. 1, pp. 15–26, 2020.
- [49] Z. Liu, Y. Lin, Y. Cao, H. Hu, Y. Wei, Z. Zhang, S. Lin, and B. Guo, "Swin transformer: Hierarchical vision transformer using shifted windows," in *ICCV*, 2021, pp. 10 012–10 022.
- [50] S. Ren, X. Yang, S. Liu, and X. Wang, "Sg-former: Self-guided transformer with evolving token reallocation," in *ICCV*, 2023, pp. 6003–6014.
- [51] J. Deng, W. Dong, R. Socher, L.-J. Li, K. Li, and L. Fei-Fei, "Imagenet: A large-scale hierarchical image database," in *CVPR*, 2009, pp. 248–255.
- [52] T.-Y. Lin, P. Dollár, R. Girshick, K. He, B. Hariharan, and S. Belongie, "Feature pyramid networks for object detection," in *CVPR*, 2017, pp. 2117–2125.
- [53] Z. Hu, M. Zhen, X. Bai, H. Fu, and C.-I. Tai, "Jsenet: Joint semantic segmentation and edge detection network for 3D point clouds," in *ECCV*, 2020, pp. 222–239.
- [54] X. Wu, Y. Lao, L. Jiang, X. Liu, and H. Zhao, "Point transformer v2: Grouped vector attention and partition-based pooling," *NeurIPS*, vol. 35, pp. 33 330–33 342, 2022.
- [55] X. Wu, L. Jiang, P.-S. Wang, Z. Liu, X. Liu, Y. Qiao, W. Ouyang, T. He, and H. Zhao, "Point transformer v3: Simpler faster stronger," in *CVPR*, 2024, pp. 4840–4851.
- [56] H. Ran, J. Liu, and C. Wang, "Surface representation for point clouds," in *CVPR*, 2022, pp. 18 942–18 952.
- [57] O. Ronneberger, P. Fischer, and T. Brox, "U-net: Convolutional networks for biomedical image segmentation," in *MICCAI*, 2015, pp. 234–241.
- [58] K. Simonyan and A. Zisserman, "Very deep convolutional networks for large-scale image recognition," *arXiv preprint arXiv:1409.1556*, 2014.